Supporting Information

Phosphate-binding protein-loaded iron oxide particles:
Adsorption performance for phosphorus removal and recovery from water

Faten B. Hussein[1], Andrew H. Cannon[2], Justin M. Hutchison[3], Christopher B. Gorman[4],

Yaroslava G. Yingling[2], Brooke K. Mayer[1*]

[1] Department of Civil, Construction and Environmental Engineering, Marquette University, 1637

West Wisconsin Avenue, Milwaukee, WI, 53233, USA

[2] Department of Materials Science and Engineering, North Carolina State University, 911

Partners Way, Raleigh, NC, 27695, USA

[3] Department Civil, Environmental & Architectural Engineering, University of Kansas, 1530 W.

15th St., Lawrence, KS, 66045, USA

[4] Department of Chemistry, North Carolina State University, Box 8204, Raleigh, NC, 27695,

USA

Emails:

Faten Hussein: faten.hussein@marquette.edu

Andrew Cannon: ahcannon@ncsu.edu

Justin Hutchison: jhutch@ku.edu

Christopher Gorman: cbgorman@ncsu.edu

Yaroslava Yingling: yara_yingling@ncsu.edu

*Corresponding author email: brooke.mayer@marquette.edu and phone: 414-288-2161

The supporting information includes four sections:

- S1 provides characteristics of the tertiary wastewater effluent sample.
- S2 provides a transmission electron microscopy (TEM) image showing the NHS-activated magnetic IOPs.
- S3 describes the adsorption kinetic models for P_i using PBP-IOPs.
- S4 details the theoretical calculations used to explore the influence of protein and substate parameters on phosphate adsorption capacity.

S1. Wastewater Effluent Characterization

The wastewater effluent parameters are shown in Table S1.

Table S1. Tertiary wastewater effluent parameters from the South Shore Water Reclamation Facility in Oak Creek, WI. Each measurement was performed in triplicate.

Parameter*	Average ± 1 Standard Deviation	Unit
Total Suspended Solid (TSS)	16 ±3	mg L^{-1}
Dissolved Organic Carbon (DOC)	9.2 ±0.1	mg-C L^{-1}
Total Hardness	327 ±10	mg L^{-1} as CaCO$_3$
Alkalinity	180 ±10	mg L^{-1} as CaCO$_3$
Chloride	460 ±10	mg L^{-1}
Phosphate	1.2 ±0.1	mg PO_4^{3-} L^{-1}
Nitrate	8.0 ±0.05	mg NO_3^{-} L^{-1}
Sulfate	224 ±0.13	mg SO_4^{2-} L^{-1}
Hydrogen Sulfide	0	mg S^{2-} L^{-1}
pH	7.13 ±0.1	---

* TSS was measured in accordance with Method 2540D from Standard Methods for the Examination of Water and Wastewater (1). DOC was measured in accordance with U.S. EPA Method 415.3 using a Shimadzu TOC-V$_{CSN}$. Other parameters were measured using Single Parameter Test Kits from the Hach Company (Loveland, CO).

S2. Transmission Electron Microscopy (TEM) of NHS-IOPs
A TEM image showing the NHS-activated magnetic IOPs is shown in Figure S1.

Figure S1. Transmission electron microscopy image of BcMag^{TM} NHS-activated magnetic IOPs (image shared by the material supplier, Bioclone Inc., USA). The TEM image depicts the silica shell surrounding the iron oxide particles.

S3. Adsorption Kinetics

Figure S2 shows the linearized pseudo second-order phosphate adsorption kinetics using PBP-IOPs. Figure S3 shows the linearized pseudo first-order phosphate adsorption kinetics using PBP-IOPs.
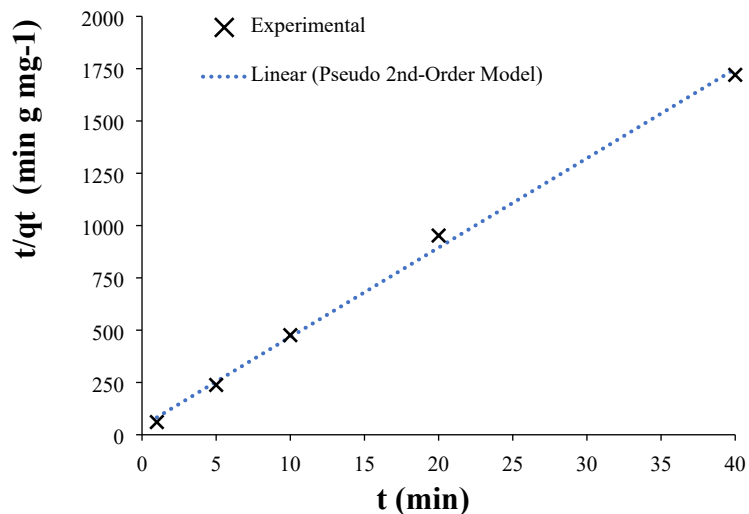
Figure S2. Linearized pseudo second-order P_i adsorption kinetics using the PBP-IOPs at neutral pH and 20 °C. Best fit model parameters: $k_2 = 45.4$ g mg^{-1}min^{-1}, $q_e = 0.023$ mg g^{-1}.
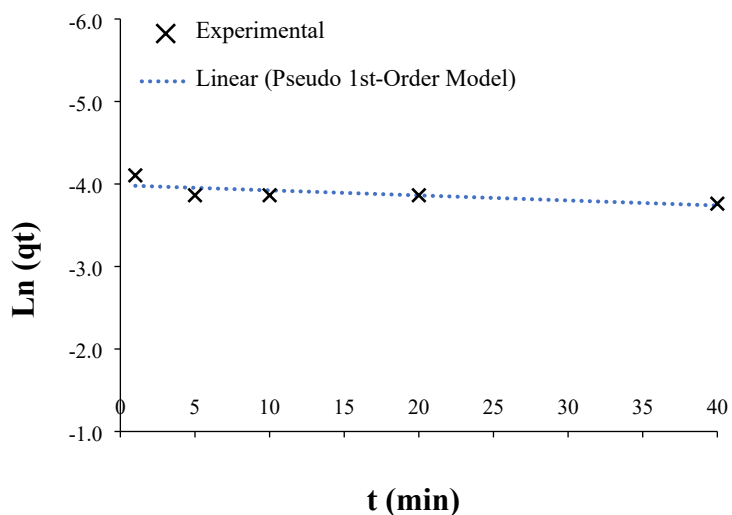
Figure S3. Linearized pseudo first-order P_i adsorption kinetics using the PBP-IOPs at neutral pH and 20 °C. Best fit model parameters: $k_1 = 0.0061$ min^{-1}, $q_e = 0.019$ mg g^{-1}.

S4. Calculation of theoretical capacity
Theoretical estimates of P_i adsorption were performed to assess the relative influence of the protein (or peptide) and the particle on which the protein was immobilized. All estimates were made assuming the particle and the PBP or peptide could be modeled as spherical particles. We recognize that these modeling scenarios do not fully represent reality (e.g., spherical particle modeling, neglecting particle curvature, etc.); however, these back-of-the-envelope theoretical estimations enable scenario comparisons and inform directions for fruitful future developments.

S4.1. Calculation of increases in surface area per mass
This set of calculations modeled the impact of changes in the surface area per mass ratio of the PBP-based adsorbent. Two different scenarios were explored: 1) P_i capacity limited by theoretical NHS ligand density (ligand-based) on the particle surface and 2) P_i capacity limited by the physical space taken up by the PBP (footprint-based).

S4.1.1. Ligand-based calculations
Ligand-based calculations were made based on the maximum NHS ligand density reported by the particle manufacturer (either for IOPs or Sepharose resin). This approach assumed that the number of NHS ligands (and therefore coupled PBP) was directly proportional to changes in the surface area to mass ratio (and that all other properties remained the same as the baseline IOP or NHS scenarios). The surface area to mass ratio of the particles was calculated as the surface area divided by particle volume and density, simplified as Eq. S1.

$$\left(\frac{SA}{m}\right) = \frac{3*10^6}{r_{particle}*\rho_{particle}} \quad \text{Eq. S1}$$

Where (SA/m) = surface area to mass ratio ($m^2 \, g^{-1}$), $r_{particle}$ = radius of the particle (µm), $\rho_{particle}$ = density of the particle ($5.24 \times 10^6 \, g \, m^{-3}$ for IOP, $0.7 \times 10^6 \, g \, m^{-3}$ for Sepharose resin) ($g \, m^{-3}$), and 10^6 accounts for unit conversions between µmol and mol.

The theoretical maximum number of PBPs on the particle was calculated using Eq. S2, assuming proportional NHS density to particle surface area and 1:1 molar PBP binding to NHS.

$$q_{PBP} = \frac{MW_{PBP}*\rho_{NHS}}{10^6}\left(\frac{\left(SA/m\right)}{\left(SA/m\right)_{baseline}}\right) \quad \text{Eq. S2}$$

Where q_{PBP} = capacity of PBP (g PBP (g particle)$^{-1}$), MW_{PBP} = molecular weight of the PBP = 35,000 g PBP (mol PBP)$^{-1}$, ρ_{NHS} = maximum NHS ligand density reported by the particle manufacturer = 250 µmol NHS (g IOP)$^{-1}$ or 32.8 µmol NHS (g Sepharose bead)$^{-1}$, (SA/m) is the ratio of surface area to mass compared to the baseline ratio of surface area to mass for the particle ($m^2 \, g^{-1}$), and 10^6 accounts for unit conversions between µmol and mol.

To convert the number of PBP on the particle to the P_i-binding capacity, Eq. S3 was used.

$$q_{PO4} = q_{PBP} * \frac{MW_{PO4}}{MW_{PBP}} * 10^3 \quad \text{Eq. S3}$$

Where q_{PO4} = capacity of PO_4 (mg PO_4 (g particle)$^{-1}$), q_{PBP} = capacity of PBP (g PBP (g particle)$^{-1}$), MW_{PO4} = 94.97 g PO_4 mol^{-1}, MW_{PBP} = molecular weight of the PBP = 35,000 g PBP (mol PBP)$^{-1}$, and 10^3 accounts for unit conversions between mg and g.

S4.1.2. Footprint-based calculations

Eq. S4 was used to estimate the number of proteins or peptides that could physically fit on the surface of the particle assuming that the spherical particle's surface was completely filled with peptides (neglecting the impact of curvature).

$$N_{PBP} = \frac{SA_{particle}}{A_{X,PBP}} = \frac{4\pi r^2_{particle}}{\pi r^2_{PBP}} \quad \text{Eq. S4}$$

Where N_{PBP} = number of PBP on the particle surface, $SA_{particle}$ = surface area of the particle (μm^2), $A_{X,PBP}$ = cross-sectional area of PBP protein (μm^2), $r_{particle}$ = radius of the particle (μm), r_{PBP} = radius of PBP protein (3.45×10^{-3} μm).

To convert the number of peptides on the particle surface to the P_i-binding capacity (assuming 1:1 molar peptide binding to NHS), Eq. S5 was used.

$$q_{PO4} = \frac{N_{PBP} * MW_{PO4} * 10^3}{6.02 * 10^{23} \frac{PBP}{mol} * \left(\frac{4}{3}\pi r^3_{particle}\right) * \rho_{particle}} \quad \text{Eq. S5}$$

Where q_{PO4} = capacity of PO_4 (mg PO_4 (g particle)$^{-1}$), N_{PBP} = number of PBP on the particle surface, MW_{PO4} = 94.97 g PO_4 mol^{-1}, $r_{particle}$ = radius of the particle (m), $\rho_{particle}$ = density of the particle (5.24×10^6 g m^{-3} for IOP, 0.7×10^6 g m^{-3} for Sepharose resin) (g m^{-3}), and 10^3 accounts for unit conversions between mg and g.

S4.2. Calculation of the effects of PBP size reduction

The PBP size reduction scenario modeled the impact of substituting a PO_4-selective peptide sequence for the full PBP. This approach assumed that peptides (ranging in size from PBP's PO_4-binding site diameter, 4 Å, up to the size of the PBP at 69 Å) 1) retained 1:1 PO_4-binding and 2) the mass of the peptide binding sequence decreased proportionally to the change in size (radius).

Two different scenarios were explored: 1) P_i capacity limited by theoretical NHS ligand density (ligand-based) on the particle surface and 2) P_i capacity limited by the physical space taken up by the protein/peptide binding sequence (footprint-based).

S4.2.1. Ligand-based calculations

Ligand-based calculations were made based on the maximum NHS ligand density reported by the particle manufacturer (either for IOPs or Sepharose resin). The theoretical maximum number of PBP on the particle was calculated using Eq. S6, assuming 1:1 molar PBP binding to NHS.

$$q_{PBP} = \frac{MW_{PBP} * \rho_{NHS}}{10^6} \quad \text{Eq. S6}$$

Where q_{PBP} = capacity of PBP (g PBP (g particle)$^{-1}$), MW_{PBP} = molecular weight of the PBP = 35,000 g PBP (mol PBP)$^{-1}$, ρ_{NHS} = maximum NHS ligand density reported by the particle manufacturer = 250 µmol NHS (g IOP)$^{-1}$ or 32.8 µmol NHS (g Sepharose bead)$^{-1}$, and 10^6 accounts for unit conversions between µmol and mol.

To convert the number of PBP on the particle to the P_i-binding capacity, Eq. S7 was used.

$$q_{PO4} = MW_{PBP} * \frac{r_{pep}}{r_{PBP}} * MW_{PO4} * 10^3 \quad \text{Eq. S7}$$

Where q_{PO4} = capacity of PO$_4$ (mg PO$_4$ (g particle)$^{-1}$), MW_{PBP} = molecular weight of the PBP = 35,000 g PBP (mol PBP)$^{-1}$, r_{pep} = radius of the peptide (nm), r_{PBP} = radius of PBP = 3.45 nm, MW_{PO4} = 94.97 g PO$_4$ mol^{-1}, and 10^3 accounts for unit conversions between mg and g.

S4.2.2. Footprint-based calculations

Eq. S8 was used to estimate the number of proteins or peptides that could physically fit on the surface of the particle assuming that the spherical particle's surface was completely filled with peptides (neglecting the impact of curvature).

$$N_{pep} = \frac{SA_{particle}}{A_{X,pep}} = \frac{4\pi r_{particle}^2}{\pi r_{pep}^2} \quad \text{Eq. S8}$$

Where N_{pep} = number of peptides (or PBP proteins) on the particle surface, $SA_{particle}$ = surface area of the particle (µm^2), $A_{X,pep}$ = cross-sectional area of the peptide (or PBP protein) (µm^2), $r_{particle}$ = radius of the particle (µm), r_{pep} = radius of the peptide (or PBP protein) (µm).

To convert the number of peptides on the particle surface to the P_i-binding capacity (assuming 1:1 molar peptide binding to NHS), Eq. S9 was used.

$$q_{PO4} = \frac{N_{pep} * MW_{PO4} * 10^3}{6.02 * 10^{23} \frac{pep}{mol} * \left(\frac{4}{3}\pi r_{particle}^3\right) * \rho_{particle}} \quad \text{Eq. S9}$$

Where q_{PO4} = capacity of PO$_4$ (mg PO$_4$ (g particle)$^{-1}$), N_{pep} = number of peptides (or PBP proteins) on the particle surface, MW_{PO4} = 94.97 g PO$_4$ mol^{-1}, $r_{particle}$ = radius of the particle (m), $\rho_{particle}$ = density of the particle (5.24x10^6 g m^{-3} for IOP, 0.7x10^6 g m^{-3} for Sepharose resin) (g m^{-3}), and 10^3 accounts for unit conversions between mg and g.

S4.2.3. Capacity comparisons

To contextualize our theoretical calculations of PBP adsorbent capacity relative to P_i adsorption performance using other adsorbents reported in the literature, we compared values to those shown in Table S2. Figure 6 in the main text illustrates the comparisons.

Table S2. Literature reports of P_i adsorption capacity (reported based on Langmuir isotherm modeling).

Quartile	Adsorbent	Capacity, mg PO_4 (g bead)$^{-1}$	Reference
1	RC-BOFS (0.8 – 2.3 mm)	0.4	(2)
	NFS	0.5	(3)
	HA-MNP	3	(4)
	FMS-0.1 La	6.1	(5)
	NLZ	7.7	(6)
	La-Z	8	(6)
	Fe-Al	8.2	(7)
	Hydrogel beads	11.7	(8)
	$ZrO_2@SiO_2@Fe_3O_4$	12	(9)
	Mg-Biochar	13.2	(10)
	GO-Zr	13.2	(11)
2	MG@La	16.6	(12)
	Aluminum hydroxide	19.8	(13)
	RHB	19.9	(14)
	Bauxite	20.6	(15)
	Fe-GAC	21.8	(16)
	ACF-Zr-Fe	29.1	(17)
	ZnFeZR-adsorbent	32.2	(18)
	Diethylamine Zr-OH	38	(19)
	Magnetic Fe-Zr	41.9	(20)
3	Zr hydroxide	46.9	(21)
	am-ZrO_2	48.5	(22)
	N-Ethylmethylamine Zr-OH	51.8	(19)
	Akaganeite	51.8	(23)
	Magnetic Fe-Zr	54.8	(20)
	Fe-Al (Mesoporous spheres)	61.5	(7)
	Akaganeite (β-FeOOH)	71.5	(23)
	Fe-Zr	76.4	(24)
	Pure-Zr-OH	79.1	(19)
	Fe-La	90.5	(25)

	CuFe$_2$O$_4$-2N-La	91.4	(26)
	Fe-Zr	102.4	(24)
	Fe-Cu	107.9	(27)
	Dimethylamine Zr-OH	110	(19)
4	Fe-Mn	110.4	(28)
	Fe-Cu	122.0	(27)
	Fe$_3$O$_4$@ASC	133	(29)
	MOD	149	(30)
	Al-Mn	183.4	(31)
	l-Y(OH)$_3$	244	(32)

References

1. APHA. Standard methods for the examination of water and wastewater. 21st ed. Washington, D.C.: American Public Health Association; 2005.

2. Park JH, Wang JJ, Kim SH, Cho JS, Kang SW, Delaune RD, et al. Phosphate removal in constructed wetland with rapid cooled basic oxygen furnace slag. Chemical Engineering Journal. 2017 Nov;327:713–24.

3. Wang W, Ma C, Zhang Y, Yang S, Shao Y, Wang X. Phosphate adsorption performance of a novel filter substrate made from drinking water treatment residuals. Journal of Environmental Sciences. 2016 Jul;45:191–9.

4. Rashid M, Price NT, Gracia Pinilla MÁ, O'Shea KE. Effective removal of phosphate from aqueous solution using humic acid coated magnetite nanoparticles. Water Res. 2017 Oct;123:353–60.

5. Huang W, Yu X, Tang J, Zhu Y, Zhang Y, Li D. Enhanced adsorption of phosphate by flower-like mesoporous silica spheres loaded with lanthanum. Microporous and Mesoporous Materials. 2015 Nov;217:225–32.

6. He Y, Lin H, Dong Y, Wang L. Preferable adsorption of phosphate using lanthanum-incorporated porous zeolite: Characteristics and mechanism. Appl Surf Sci. 2017 Dec;426:995–1004.

7. Sousa AF de, Braga TP, Gomes ECC, Valentini A, Longhinotti E. Adsorption of phosphate using mesoporous spheres containing iron and aluminum oxide. Chemical Engineering Journal. 2012 Nov;210:143–9.

8. Wan J, Tao T, Zhang Y, Liang X, Zhou A, Zhu C. Phosphate adsorption on novel hydrogel beads with interpenetrating network (IPN) structure in aqueous solutions: kinetics, isotherms and regeneration. RSC Adv. 2016;6(28):23233–41.

9. Fang L, Wu B, Lo IMC. Fabrication of silica-free superparamagnetic ZrO2@Fe3O4 with enhanced phosphate recovery from sewage: Performance and adsorption mechanism. Chemical Engineering Journal. 2017 Jul;319:258–67.

10. Yao Y, Gao B, Chen J, Yang L. Engineered Biochar Reclaiming Phosphate from Aqueous Solutions: Mechanisms and Potential Application as a Slow-Release Fertilizer. Environ Sci Technol. 2013 Aug 6;47(15):8700–8.

11. Zong E, Wei D, Wan H, Zheng S, Xu Z, Zhu D. Adsorptive removal of phosphate ions from aqueous solution using zirconia-functionalized graphite oxide. Chemical Engineering Journal. 2013 Apr;221:193–203.

12. Rashidi Nodeh H, Sereshti H, Zamiri Afsharian E, Nouri N. Enhanced removal of phosphate and nitrate ions from aqueous media using nanosized lanthanum hydrous doped on magnetic graphene nanocomposite. J Environ Manage. 2017 Jul;197:265–74.

13. Chen YSR, Butler JN, Stumm W. Adsorption of phosphate on alumina and kaolinite from dilute aqueous solutions. J Colloid Interface Sci. 1973 May;43(2):421–36.

14. Kizito S, Luo H, Wu S, Ajmal Z, Lv T, Dong R. Phosphate recovery from liquid fraction of anaerobic digestate using four slow pyrolyzed biochars: Dynamics of adsorption, desorption and regeneration. J Environ Manage. 2017 Oct;201:260–7.

15. Altundoğan HS, Tümen F. Removal of phosphates from aqueous solutions by using bauxite. I: Effect of pH on the adsorption of various phosphates. Journal of Chemical Technology & Biotechnology. 2002 Jan 3;77(1):77–85.

16. Suresh Kumar P, Prot T, Korving L, Keesman KJ, Dugulan I, van Loosdrecht MCM, et al. Effect of pore size distribution on iron oxide coated granular activated carbons for phosphate adsorption – Importance of mesopores. Chemical Engineering Journal [Internet]. 2017;326:231–9. Available from: http://dx.doi.org/10.1016/j.cej.2017.05.147

17. Xiong W, Tong J, Yang Z, Zeng G, Zhou Y, Wang D, et al. Adsorption of phosphate from aqueous solution using iron-zirconium modified activated carbon nanofiber: Performance and mechanism. J Colloid Interface Sci. 2017 May;493:17–23.

18. Drenkova-Tuhtan A, Schneider M, Franzreb M, Meyer C, Gellermann C, Sextl G, et al. Pilot-scale removal and recovery of dissolved phosphate from secondary wastewater effluents with reusable ZnFeZr adsorbent @ Fe3O4/SiO2 particles with magnetic harvesting. Water Res [Internet]. 2017;109:77–87. Available from: http://dx.doi.org/10.1016/j.watres.2016.11.039

19. Luo X, Wu X, Reng Z, Min X, Xiao X, Luo J. Enhancement of Phosphate Adsorption on Zirconium Hydroxide by Ammonium Modification. Ind Eng Chem Res. 2017 Aug 30;56(34):9419–28.

20. Long F, Gong JL, Zeng GM, Chen L, Wang XY, Deng JH, et al. Removal of phosphate from aqueous solution by magnetic Fe–Zr binary oxide. Chemical Engineering Journal. 2011 Jul;171(2):448–55.

21. Johir MAH, Pradhan M, Loganathan P, Kandasamy J, Vigneswaran S. Phosphate adsorption from wastewater using zirconium (IV) hydroxide: Kinetics, thermodynamics and membrane filtration adsorption hybrid system studies. J Environ Manage. 2016 Feb;167:167–74.

22. Su Y, Cui H, Li Q, Gao S, Shang JK. Strong adsorption of phosphate by amorphous zirconium oxide nanoparticles. Water Res. 2013 Sep;47(14):5018–26.

23. Genz A, Kornmüller A, Jekel M. Advanced phosphorus removal from membrane filtrates by adsorption on activated aluminium oxide and granulated ferric hydroxide. Water Res. 2004 Sep;38(16):3523–30.

24. Ren Z, Shao L, Zhang G. Adsorption of Phosphate from Aqueous Solution Using an Iron–Zirconium Binary Oxide Sorbent. Water Air Soil Pollut. 2012 Sep 5;223(7):4221–31.

25. Liu J, Zhou Q, Chen J, Zhang L, Chang N. Phosphate adsorption on hydroxyl–iron–lanthanum doped activated carbon fiber. Chemical Engineering Journal. 2013 Jan;215–216:859–67.

26. Gu W, Li X, Xing M, Fang W, Wu D. Removal of phosphate from water by amine-functionalized copper ferrite chelated with La(III). Science of The Total Environment. 2018 Apr;619–620:42–8.

27. Li G, Gao S, Zhang G, Zhang X. Enhanced adsorption of phosphate from aqueous solution by nanostructured iron(III)–copper(II) binary oxides. Chemical Engineering Journal. 2014 Jan;235:124–31.

28. Zhang C, Chen Y. Simultaneous Nitrogen and Phosphorus Recovery from Sludge-Fermentation Liquid Mixture and Application of the Fermentation Liquid To Enhance Municipal Wastewater Biological Nutrient Removal. Environ Sci Technol. 2009 Aug 15;43(16):6164–70.

29. Jiang D, Amano Y, Machida M. Removal and recovery of phosphate from water by a magnetic Fe 3 O 4 @ASC adsorbent. J Environ Chem Eng. 2017 Oct;5(5):4229–38.

30. Xie F, Wu F, Liu G, Mu Y, Feng C, Wang H, et al. Removal of Phosphate from Eutrophic Lakes through Adsorption by in Situ Formation of Magnesium Hydroxide from Diatomite. Environ Sci Technol. 2014 Jan 7;48(1):582–90.

31. Wu K, Liu T, Ma C, Chang B, Chen R, Wang X. The role of Mn oxide doping in phosphate removal by Al-based bimetal oxides: adsorption behaviors and mechanisms. Environmental Science and Pollution Research. 2014 Jan 2;21(1):620–30.

32. Kim M, Kim H, Byeon SH. Layered Yttrium Hydroxide *l* -Y(OH) $_3$ Luminescent Adsorbent for Detection and Recovery of Phosphate from Water over a Wide pH Range. ACS Appl Mater Interfaces. 2017 Nov 22;9(46):40461–70.